Title: ***The Zn, S, and Cl isotope compositions of mare basalts: implications for the effects of eruption style and pressure on volatile element stable isotope fractionation on the Moon***

Word count: 6,400

Authors and Affiliations: Anthony GARGANO[1,2,*], James DOTTIN[3], Sean S. HOPKINS[4], Zachary SHARP[1,2], Charles SHEARER[5], Alex N. HALLIDAY[4,6], Fiona LARNER[4], James FARQUAR[3,7], and Justin SIMON[8].

[1]Department of Earth and Planetary Sciences, University of New Mexico, Albuquerque, New Mexico 87131-0001, USA

[2]Center for Stable Isotopes, University of New Mexico, Albuquerque, New Mexico 87131-0001, USA

[3]Department of Geology, University of Maryland, College Park, MD, 20742, USA

[4]Department of Earth Sciences, University of Oxford, OX1 3AN, United Kingdom

[5]Institute of Meteoritics, University of New Mexico, Albuquerque, New Mexico 87131-0001, USA

[6]The Earth Institute, Columbia Climate School, Columbia University, New York, NY 10025, USA

[7]Earth System Science Interdisciplinary Center, College Park, MD 20742, USA

[8]Center for Isotope Cosmochemistry and Geochronology, Astromaterials Research and Exploration Science Division, The Lyndon B. Johnson Space Center, National Aeronautics and Space Administration, Houston, TX 77058

[*]Corresponding author. E-mail: agargano@unm.edu

Abstract:

We compare the stable isotope compositions of Zn, S, and Cl for Apollo mare basalts to better constrain the sources and timescales of lunar volatile loss. Mare basalts have broadly elevated, yet limited, ranges in $\delta^{66}Zn$, $\delta^{34}S$, and $\delta^{37}Cl_{SBC+WSC}$ values of 1.27 ± 0.71, 0.55 ± 0.18,

and 4.1 ± 4.0‰, respectively compared to the silicate Earth at 0.15, -1.28‰, and 0‰, respectively. We find that the Zn, S, and Cl isotope compositions are similar between the low and high-Ti mare basalts, providing evidence of a geochemical signature in the mare basalt source region that is inherited from lunar formation and magma ocean crystallization. The uniformity of these compositions implies mixing following mantle overturn, as well as minimal changes associated with subsequent mare magmatism. Degassing of mare magmas and lavas did not contribute to the large variations in Zn, S, and Cl isotope compositions found in some lunar materials (i.e., 15‰ in δ^{66}Zn, 60‰ in δ^{34}S, and 30‰ in δ^{37}Cl). This reflects magma sources that experienced minimal volatile loss due to high confining pressures that generally exceeded their equilibrium saturation pressures. Alternatively, these data indicate effective isotopic fractionation factors were near unity.

Our observations of S isotope compositions in mare basalts contrast to those for picritic glasses (Saal & Hauri 2021) which vary widely in S isotope compositions from -14.0 to 1.3‰ explained by extensive degassing of picritic magmas under high P/P_{Sat} values (> 0.9) during pyroclastic eruptions. The difference in the isotope compositions of picritic glass beads and mare basalts may result from differences in effusive (mare) and explosive (picritic) eruption styles wherein the high gas contents necessary for magma fragmentation would result in large effective isotopic fractionation factors during degassing of picritic magmas. Additionally, in highly vesiculated basalts, the δ^{34}S and δ^{37}Cl values of apatite grains are higher and more variable than the corresponding bulk-rock values. The large isotopic range in the vesiculated samples is explained by late-stage low-pressure 'vacuum' degassing ($P/P_{Sat} \sim 0$) of mare lavas wherein vesicle formation and apatite crystallization took place post-eruption. Bulk-rock mare basalts were seemingly unaffected by vacuum degassing. Degassing of mare lavas only became important in the final stages of crystallization recorded in apatite - potentially facilitated by cracks/fractures in

the crystallizing flow. We conclude that samples with wide-ranging volatile element isotope compositions are likely explained by localized processes which do not represent the bulk-Moon.

Keywords: zinc isotopes, sulfur isotopes, chlorine isotopes, lunar volatiles, degassing

Introduction:

Compared to the Earth, the Moon is extensively depleted in volatile elements and preserves a wide range of volatile-element stable isotope compositions such as for H, Cl, Zn, and S (Barnes et al., 2014; Faircloth et al., 2020; Moynier et al., 2006; Rees and Thode, 1974; Saal and Hauri, 2021; Sharp et al., 2010). These distinct chemical features are largely consistent with lunar formation from a Giant Impact (Charnoz et al., 2021; Paniello et al., 2012; Wing and Farquhar, 2015), in which a Mars-sized impactor collided with the proto-Earth forming a silicate-vapor disk which would later condense to form the Moon (Canup et al., 2015). Partial condensation of the proto-lunar disk (**PLD**) is consistent with volatile depletion (Canup et al., 2015; Lock et al., 2018), and many isotopic anomalies in moderately volatile stable isotope systems can be explained by vapor-drainage of the PLD to the proto-Earth (Nie and Dauphas, 2019). The explanation for the larger ranges in the isotopic compositions of highly volatile elements, however, remains elusive. This difficulty stems from the fact that the Moon underwent multiple events capable of causing isotopic fractionation of highly volatile elements such as the Giant Impact (Paniello et al., 2012), tidally-assisted hydrodynamic escape (Charnoz et al., 2021), degassing from the Lunar Magma Ocean (**LMO**)(Tang and Young, 2020), and later mare volcanism, which covered ~17% of the lunar surface in basaltic lava flows and pyroclastics (Head and Wilson, 2017; Shearer et al., 2006).

Mechanisms to explain highly volatile element stable isotope anomalies include degassing from the LMO (Boyce et al., 2018; Boyce et al., 2015), degassing facilitated by crust-breaching

impacts (Barnes et al., 2016; McCubbin and Barnes, 2020), volcanic degassing (Sharp et al., 2010) and devolatilization associated with the Giant Impact (Gargano et al., 2020). The importance of early, global degassing must take into account the rapid solidification of the LMO surface layer 'lid' which would presumably reduce vapor-loss (Barnes et al., 2016; Gargano et al., 2020), and occurred rapidly within thousands of years (Elkins-Tanton et al., 2011). In addition, recent isotopic modeling has shown that the silicate-vapor above the LMO would be in isotopic equilibrium with the magma ocean, resulting in limited isotopic fractionation (Tang and Young, 2020). Subsequent mare magmatism was comparatively prolonged, occurring from 3.9 to 3.1 Ga (Hiesinger et al., 2011), which would feasibly result in further extents of degassing.

The degree to which these individual volatile-loss mechanisms contribute to lunar volatile element stable isotope anomalies is poorly constrained. Are they inherited from the Giant Impact, the LMO, or are they a direct result from degassing during mare volcanism? Addressing the origin of volatile element stable isotope anomalies has been hampered by the lack of a resolvable relationship between a given volatile element's concentration and its isotopic composition (i.e. [Cl] and δ^{37}Cl). In this work we address this problem by combining three volatile element stable isotope systems which differ in volatility and geochemical affinity. Our intent in the combination of these measurement techniques is to interrogate the relationships between volatile element stable isotope compositions and better understand the sources thereof. We thus measured the Zn, S, and Cl in the same lunar mare basalts, taking into account the well-recognized intra- and intersample isotopic variability in lunar materials (Lock et al., 2020). If the isotopic anomalies for these elements relative to the Earth are a product of early, global processes during lunar formation (Giant Impact and/or subsequent degassing of the LMO), then their isotopic compositions should not change during subsequent magmatic processes such as fractional crystallization within the LMO

and localized volcanic degassing. In contrast, if mare volcanism significantly contributed to lunar volatile loss and isotope fractionation, then the mare basalt suite should have a range of isotopic compositions associated with differing volatile contents and other volatile element stable isotope compositions.

Results:

We measured a suite of mare basalts for Zn, S and Cl isotope analyses. Quadruple S isotope measurements were made using gas source mass spectrometry at the University of Maryland (Fig. 1), and Zn concentration and isotopic compositions were measured using double-spiking and MC-ICPMS at Oxford University (Fig. 2) (see Methods for details of analysis). The halogen contents and δ^{37}Cl values of these samples were measured at the Center for Isotope Cosmochemistry and Geochronology at NASA JSC and the University of New Mexico and have been previously presented (Fig. 3) (Gargano et al. 2020). Chlorine analyses are separated into water-soluble chloride (**WSC**) and structurally-bound chloride (**SBC**) fractions.

Of the samples measured in this work, the δ^{66}Zn values (‰ vs. JMC-Lyon) range from -9.6 to +1.9‰ with concentrations from 0.8 to 6.7 ppm, and δ^{34}S values (‰ vs. CDT) range from 0.07 to 0.93‰ with concentrations from 500 to 2500 ppm (Table 1). The Zn contents of high and low-Ti basalts average 2.48 ± 1.96 and 1.04 ± 0.30 ppm, respectively and δ^{66}Zn values average -0.49 ± 4.0 and 0.93 ± 1.3‰, respectively (± indicates 1σ standard deviation). Sulfur contents of high and low-Ti basalts average 1480 ± 490 and 700 ± 258 ppm with δ^{34}S values of 0.63 ± 0.21 and 0.52 ± 0.27‰, respectively. High and low-Ti basalts have Δ^{33}S and Δ^{36}S values of -0.0012 ± 0.01, 0.0046 ± 0.01, and 0.0184 ± 0.182, 0.0737 ± 0.189‰, respectively. The slight differences in the

$\Delta^{33}S$ and $\Delta^{36}S$ values between the low and high-Ti mare basalts are not significant relative to the estimated uncertainties of 0.008 and 0.3‰, respectively.

The differences for the $\delta^{66}Zn$ and $\delta^{34}S$ values between low and high-Ti mare basalts measured in this work are not statistically significant (unpaired *t* test results: $\delta^{66}Zn$ $t_{(18)} = 2.047$, $P = 0.0575$; $\delta^{34}S$ $t_{(18)} = 0.9820$, $P = 0.3407$). Previous results for mare basalts average $\delta^{66}Zn = 1.27 \pm 0.71$‰ (Moynier et al., 2006; Paniello et al., 2012), which is indistinguishable from our average of 1.31 ± 0.44 (excluding 10017) and $\delta^{34}S$ values of 0.55 ± 0.18‰ (Rees and Thode, 1974; Wing and Farquhar, 2015), compared to our values of 0.59 ± 0.22‰ (Figs. 4 & 5). The $\delta^{37}Cl_{SBC}$ and $\delta^{37}Cl_{WSC}$ values are similarly indistinguishable between the low and high-Ti basalts and range from 7.3 ± 3.5 and 1.8 ± 2.5‰, respectively with concentrations from 1.1 to 5.8, and 1.9 to 10 ppm, respectively (Fig. 6). No clear correlation is present in the $\delta^{66}Zn$, $\delta^{34}S$, and $\delta^{37}Cl_{SBC, WSC}$ values of mare basalts (Fig. 7).

In contrast to the isotope data, there are clear differences in the S and Zn contents of low and high-Ti basalts. High-Ti basalts contain an average of 1542 ± 462 ppm S relative to the 678 ± 180 in low-Ti basalts ($t_{(41)} = 8.6730$, $P = 0.0001$). A similar statistically significant difference holds for Zn contents, with high and low-Ti mare basalts containing an average of 2.55 ± 1.75 and 1.02 ± 0.31 ppm Zn, respectively ($t_{(38)} = 3.5550$, $P = 0.0015$). There is also a positive correlation between the F and S concentrations for the full suite of mare basalts (Fig. 8). Lastly, while the Zn, S, and Cl isotope compositions of mare basalts are generally independent of Zn, S, and halogen contents, sample 10017 with the lowest $\delta^{66}Zn$ values has far higher Zn contents than the average mare basalt.

Discussion:

The Zn, S, Cl and F contents of mare basalts:

We begin our discussion with the Zn, S, Cl and F contents and isotope compositions of mare basalts within the context of lunar mantle differentiation. Following lunar accretion, the LMO quickly solidified with 80% crystallization taking place within 1000 years (Elkins-Tanton et al., 2011). The initial ~70% of crystallization formed olivine and orthopyroxene-rich cumulates, and later plagioclase, which was positively buoyant in the LMO and produced the ferroan anorthosite (FANs) crust (Snyder et al., 1992). Further crystallization continued for 10-100 million years, forming olivine, orthopyroxene and clinopyroxene-bearing cumulates as well as ilmenite-rich cumulates at >90% crystallization (Elkins-Tanton et al., 2011; Snyder et al., 1992). Prior to complete solidification, the lunar mantle overturned due to the crystallization of dense ilmenite-rich cumulates above comparatively less-dense olivine and pyroxene-rich cumulates, mixing the lunar mantle (Elkins-Tanton et al., 2011; Shearer et al., 2006). Mare basalts represent partial melts derived from such cumulates and are generally separated into the low-Ti and high-Ti subgroupings, with the high-Ti basalts likely represent mixing between early-stage olivine & pyroxene-bearing cumulates and late-stage ilmenite-bearing cumulates respectively (Hess and Parmentier, 1995; van Kan Parker et al., 2011). Multiple saturation pressures of mare basalts range between 1-1.5 GPa, relating to source region depths of 200-300 km (Ding et al., 2018; Green et al., 1975; Kesson, 1975; Longhi, 1992; Longhi et al., 1972; Snyder et al., 1992; Walker et al., 1976; Walker et al., 1972). Mare basalts consist of numerous lava flows erupted over a period of ~300 Ma (Snyder et al., 2000). Differences, or lack thereof, in the Zn, S, and Cl contents and isotopic compositions of the mare basalt suite are expected to be related to the temporal variation between the crystallization of the cumulate source regions, subsequent magmatic processes such as differentiation and degassing, and crystallization of individual lava flows.

The magmatic compatibilities of the elements of interest are Zn > F > Cl > S. If the high-Ti basalts were sourcing a late-crystallizing component rich in incompatible elements, then we would expect to see the relative concentrations of these elements related to their magmatic compatibility. Instead, we find that the high-Ti basalts contain higher Zn (2.55 ± 1.75 and 1.02 ± 0.31) and F (28.0 ± 7.6 vs. 18.7 ± 7.6 ppm) abundances, yet similar Cl_{SBC} (2.4 ± 1.1 vs. 2.2 ± 1.4 ppm) and far higher S contents (1542 ± 462 ppm vs. 678 ± 180) compared to low-Ti basalts. As Zn is lithophile under relevant P-T and fO_2 conditions of the lunar mantle, the increased Zn content of the high-Ti basalts is likely due to Zn incorporation in the chromite component within the source region (Snyder et al., 1992) and high Zn-partitioning thereof (Davis et al., 2013). Recent work has shown F partitioning in pyroxene and olivine to be dependent on Ti contents (Potts et al., 2021), and olivine within Apollo 11 rocks is in fact Ti-rich (Brett et al., 1971), likely explaining the F vs. Ti trend observed in the mare basalt suite (Gargano et al., 2020).

Concentrations of volatiles in mare basalts may also be lowered by degassing. Renggli et al. (2017) showed with lunar gas phase modeling that at 1200 ºC, 10^{-6} bar and at IW-2, the predominant gas species are S_2, CO, and H_2 – with Zn, Cl, and F speciation of $Zn^{o}_{(g)}$, HCl, and HF, respectively (Renggli et al., 2017; Renggli and Klemme, 2021). At higher pressures (1 bar) the dominant S-speciation changes to S_2 becoming subordinate relative to H_2S and COS. As such, the amount of degassing expected from our elements of interest is S > Cl > F > Zn, in agreement with the trend of Ustunisik et al. (2015). Sulfur is likely the most readily degassed volatile followed by Cl where the vapor-melt partition coefficient (2.2 to 13-85) is influenced by the abundance of H_2O and S in the melt whereas F is unaffected (1.8) (Sigmarsson et al., 2020). Sulfur in particular is recognized to efficiently degas from basaltic melts, with some terrestrial lavas having lost up to 94% of their initial sulfur following exhumation and solidification (Bali et al., 2018; Gauthier et

al., 2016). In contrast, F and Cl are minimally lost owing to their high solubilities (several wt%) in H_2O-poor basaltic melts (Webster et al., 1999). Low Cl vapor-melt partition coefficients may also reflect the decreased role of carrier gas phases such as H_2O and SO_2 which facilitate the formation of HCl and S-Cl ligands (Sigmarsson et al., 2020; Zolotov and Matsui, 2002). The affinity for Zn in the vapor phase is more difficult to constrain, although the high Zn abundance on the coatings of volcanic glass beads is necessarily explained by Zn vaporization during lunar volcanism (Hauri et al., 2015; Ma and Liu, 2019). Lastly, the extent of degassing of these volatiles should also be reflected in their isotopic compositions.

The S, Zn, and Cl isotope composition of mare basalts:

Most bulk-rock mare basalts have generally elevated, yet limited, ranges in $\delta^{66}Zn$, $\delta^{34}S$, and $\delta^{37}Cl_{SBC+WSC}$ values (averages 1.31 ± 0.44, 0.59 ± 0.22, and 4.1 ± 4.0‰, respectively) compared to the silicate Earth (0.15, -1.28, and 0‰) (Labidi et al., 2013; Sharp et al., 2013b; Sossi et al., 2018). There are several anomalous samples that have low $\delta^{66}Zn$ values (10017, 12018, 15016, and 14053) explained by degassing and subsequent vapor deposition (Day et al., 2017; Day et al., 2020). This idea is also seen in Cl, with the particularly high $\delta^{37}Cl_{SBC, WSC}$ values in 10017-405 (9.2 and 12.6‰), 12018 (10.1 and 5.0‰), and 14053 (11.2 and 6.1‰) (Gargano et al., 2020). In the case of "Rusty Rock" 66095, which represents the 'end-member' of low $\delta^{66}Zn$ (-15‰) and high $\delta^{37}Cl_{SBC}$ and $\delta^{37}Cl_{WSC}$ values (~15‰) resulting from vapor condensation (Day et al., 2017; Shearer et al., 2014), these isotope values may reflect specific conditions such as orders of magnitude higher fCl_2 values when compared to pyroclastic gases (Renggli and Klemme, 2021). As such, these anomalous samples are unlikely to reflect primary isotopic signatures of the Moon, and instead represent secondary processes resulting from vapor condensation.

The more restricted main population of bulk-rock $\delta^{66}Zn$ and $\delta^{34}S$ values of mare basalts reflects conditions that produced limited isotope fractionation throughout LMO crystallization and degassing, as well as during later exhumation and crystallization as lava flows. If there had been isotope fractionation during LMO crystallization, then we would expect to see variable isotopic compositions between low-Ti and high-Ti basalts due to differing extents of degassing and incorporation of late-stage melts. The lack of isotopic variability between the two basalt types is consistent with the fact that $\delta^{34}S$ and $\delta^{66}Zn$ are insensitive to partial melting (Labidi and Cartigny, 2016; Wang et al., 2017), and $\delta^{66}Zn$ is minimally affected by magmatic differentiation (i.e. $\Delta^{66}Zn_{Spl\text{-}Ol} = 0.12 \pm 0.07‰$) (Chen et al., 2013; Wang et al., 2017). Sulfur isotope values are more sensitive to differentiation; at sulfide saturation $\Delta^{34}S_{FeS\text{-}melt}$ ranges from 1-2‰ at 1450 ºC (de Moor et al., 2013; Marini et al., 2011), which would leave residual silicates with low $\delta^{34}S$ values. This fractionation mechanism, however, is inconsistent with the high $\delta^{34}S$ values of mare basalts.

The effect of differentiation on Cl isotope fractionation has not been studied experimentally, although is generally assumed to be minimal given the small isotopic fractionations at high temperatures (Gargano and Sharp, 2019; Schauble et al., 2003) and the absence of multiple Cl oxidation states in magmatic systems. Instead, the low $\delta^{37}Cl_{WSC}$ ($1.8 \pm 2.5‰$) relative to the high $\delta^{37}Cl_{SBC}$ (7.3 ± 3.5) values is interpreted to reflect kinetic isotope fractionation of Cl via degassing, followed by subsequent deposition of isotopically light Cl-bearing vapor (Gargano et al., 2020; Sharp et al., 2010). It is important to note that samples with anomalously high $\delta^{37}Cl_{WSC}$ values (i.e., FANs, 66095, 10017) are necessarily sourced from a high $\delta^{37}Cl$-bearing melt in order to off-set the light isotope enrichment in the vapor phase (Gargano et al., 2020).

In total, while the concentrations of S, Zn, and Cl can change during fractional crystallization and assimilation, the only effective way to significantly modify their isotopic compositions is through extraction of the vapor phase. The variable S and Z concentrations, but effectively constant isotopic compositions for most samples suggest either that degassing of mare basalts was minimal for these elements, or that the integrated effective isotopic fractionation factor associated with degassing was near unity.

Implications for the $\Delta^{33}S$ values of mare basalts:

An important observation from our work and that presented in Wing and Farquhar (2015) is that the $\Delta^{33}S$ values of mare basalts is no different than that of the silicate Earth (where $\Delta^{33}S$ = 0‰, Labidi et al. 2013). Recent work has shown that various primitive and differentiated meteoritic materials have distinct $\Delta^{33}S$ compositions that are linked to specific parent bodies where the differences in $\Delta^{33}S$ among the parent bodies may be due to processing of sulfur in different nebular environments (Antonelli et al., 2014; Dottin III et al., 2018; Labidi et al., 2017; Rai et al., 2005; Wu et al., 2018). Furthermore, similarity in $\Delta^{33}S$ between various planetary materials (e.g. Main Group Pallasites and IIIAB iron meteorites) can be used to link the two materials to a single parent body (Dottin III et al., 2018). Although the silicate Earth and Moon have differences in $\delta^{34}S$ values, the similarity in $\Delta^{33}S$ simply suggests that they are related. Their relationship may reflect formation from materials in the same nebular environment and/or derivation from the same parent body.

Isotopic systematics of lunar volcanism:

Degassing of mare basalts occurred in the subsurface from gas exsolution during exhumation (Head and Wilson, 2017), and during second-boiling upon eruption (Wilson and Head, 2017a). If degassing occurred under vacuum conditions at the surface via a fracture network, then

254 the preferential loss of light isotopes (i.e., ^{64}Zn, ^{35}Cl, and ^{32}S) could dominate other isotopic
255 fractionation mechanisms (i.e., equilibrium fractionation between mineral phases at high
256 temperatures) and leave the residue enriched in the heavy isotope.

257 Evaporative loss under vacuum conditions is approximated by the kinetic isotope
258 fractionation factor (α_{Kin}) defined as $\sqrt{\frac{M_1}{M_2}}$ where $M_{1,2}$ are the masses of the light and heavy
259 isotopologues, respectively. For lunar gas compositions, COS and H_2S are the expected dominant
260 phases for S (Renggli et al., 2017; Renggli and Klemme, 2021). Under ideal degassing into a
261 vacuum, the fractionation of these S-bearing isotopologues yields $1000ln\alpha_{Melt\text{-}H2S,\ Melt\text{-}COS} = 28$ and
262 16‰, respectively, enriching the melt in ^{34}S. In contrast, equilibrium fractionation between these
263 vapor species and silicate melt has the opposite effect, with COS and H_2S being ^{34}S-rich relative
264 to the melt, depleting the melt in ^{34}S (Marini et al., 2011; Richet et al., 1977). This means that the
265 gas phase will vary from strongly incorporating the light isotope during vacuum degassing to
266 incorporating the heavy isotope under gas saturated, equilibrium conditions (van Kooten et al.,
267 2020). Even minimal volatile-loss under vacuum conditions should lead to wide-ranging and heavy
268 isotopic compositions regardless of which S-bearing species is dominant at any given condition
269 (i.e., P, T, fH_2, fO_2). For example, 20% S-loss as H_2S under vacuum would produce a $\delta^{34}S$ change
270 of +7‰ in the residual magma, whereas the measured range of $\delta^{34}S$ values for the entire mare
271 basalt suite is less than 2‰ (Wing and Farquhar, 2015). A similar argument also holds for Zn. As
272 such, the lack of large variations in the $\delta^{34}S$ and $\delta^{66}Zn$ values of mare basalts suggests that either
273 the integrated effective fractionation factors during degassing were near unity or alternatively, that
274 the amount of degassing itself was minimal.

275 In contrast to the mare basalts, some lunar lithologies have been shown to have extreme
276 variations in the Zn, S and Cl isotope compositions (15‰ in $\delta^{66}Zn$, 60‰ in $\delta^{34}S$, and 30‰ in

277 $\delta^{37}Cl$). These isotope values are likely explained by kinetic isotope fractionation during degassing
278 into a near-vacuum with large effective α values. The magnitude of this effect will be increased if
279 the escaping gas involve low-mass species, such as Zn^o and HCl, which lead to larger
280 fractionations than for relatively higher-mass isotopologues, such as ZnS, FeS_2 and $FeCl_2$. Low
281 molecular mass degassing is required to explain the exceptionally low Zn and high Cl isotope
282 values seen in 66095 (Rusty Rock) and some FAN samples (Gargano et al., 2020; Kato et al.,
283 2015). Interestingly, while bulk-rock mare basalts do not retain such anomalous Zn, S, or Cl
284 isotope compositions, the $\delta^{34}S$ values of picritic glass beads (**PGBs**) range from -14.0 to 1.3‰
285 (Saal and Hauri, 2021) despite the fact that they are generally petrogenetically related to the more
286 evolved mare basalts (Hauri et al., 2015). Picritic magmas are expected to have experienced limited
287 differentiation, whereas mare basalts were produced following 20-30% fractional crystallization
288 (Shearer and Papike, 1993). As such, the starkly different $\delta^{34}S$ values of the PGBs when compared
289 to mare basalts is likely explained by differences in eruption styles.
290
291 ***Isotopic consequences of pyroclastic vs. effusive mare volcanism:***
292 The initial stages of lunar volcanism are characterized by high ascent rate explosive
293 volcanic eruptions via rapid dike propagation driven by the exsolution of CO (Wilson and Head,
294 2018) and H_2 (Newcombe et al., 2019; Newcombe et al., 2017; Sharp et al., 2013a). Explosive
295 mare volcanism resulted in widespread pyroclastic deposits such as picritic glasses which were
296 fragmented during exhumation due to high gas phase volumes (~>70%) (Rutherford et al., 2017).
297 Wilson and Head (2018) describe this phase as short-lived, with a zone of pure gas extending
298 within the dike from depths from 100-200 m, above a highly vesicular foam extending to around
299 10 km. It is important to note that such dike systems are expected to be vertically extensive ranging

300 from 50-90 km, penetrating the ~30 km thick lunar crust (Wieczorek et al., 2013) and upper lunar
301 mantle (Wilson and Head, 2017b). In contrast, mare basalt volcanism consisted of more prolonged
302 events (10-100 days) with relatively slower ascent rates and fluxes (Wilson and Head, 2018). We
303 suggest these two styles or phases of volcanism represent starkly different degassing regimes. The
304 former, sampled in PGBs is extensively degassed – as evidenced by marked differences in volatile
305 contents when compared to melt inclusions (Chen et al., 2015; Hauri et al., 2011; Ni et al., 2019)
306 and exceptionally low $\delta^{34}S$ values (Saal and Hauri, 2021). The subsequently-emplaced mare
307 basalts are comparatively less degassed – seen by limited ranges in Zn, S and Cl isotope values,
308 comparatively higher Zn, S, and Cl concentrations, and the vesicular nature of several samples
309 such as 15556 and 15016.
310
311 ***Pyroclastic: Picritic Magmas.*** Saal & Hauri (2021) interpret the wide range of S contents and
312 $\delta^{34}S$ values in PGBs to result from extensive degassing under high P/P_{Sat} values. These authors
313 propose a degassing regime with an effective isotope fractionation factor of $\alpha'_{\mathrm{Kin}} =$
314 $(\alpha_{\mathrm{Kin}} - 1)\left(1 - \frac{P}{P_{Sat}}\right) + 1$, where P/P_{Sat} is equal to the effective vapor pressure of a given
315 element relative to the saturation vapor pressure (Saal and Hauri, 2021). In this scenario, a
316 crossover at $P/P_{Sat} \sim 0.86$ results in the α'_{Kin} value deviating from <1 to >1, resulting in heavy-
317 isotope loss when degassing occurs in a near-saturated medium with $P/P_{Sat} > 0.86$ and a light-
318 isotope loss when degassing occurs under low vapor pressure conditions. The crossover P/P_{Sat}
319 value depends on the appropriate proportions of degassing S-species (S_2, H_2S and COS) ranging
320 from 0.8 assuming S_2 degassing, and 0.9 with H_2S.
321 Saal & Hauri (2021) conclude that the low $\delta^{34}S$ values of PGBs requires degassing to take
322 place into a medium with $P/P_{Sat} > 0.9$. This condition is feasible within the upper levels of the

volcanic conduit given the high-gas phase volumes necessary for magma formation and PGB formation (Newcombe et al., 2017; Rutherford et al., 2017). Rutherford et al. (2017) propose that picritic magmas were rapidly exhumed from ~500 m depth to the lunar surface within 50-100s. These authors further describe the evolution of picritic magmas with 8-15% gas phase volumes at 500 m depth, rapidly increasing to 93-94% at 25 m. The high gas pressures in the upper levels of the conduit (approaching equilibrium with the melt) can explain the necessary high $\alpha'_{Kin(vapor\text{-}melt)}$ values (>1).

Importantly, the exceptionally low $\delta^{34}S$ values in PGBs requires that >80% of their initial S content was lost during degassing and it was done at a near-saturation confining pressure. This condition is feasible in pyroclastic eruption styles as exsolved volatiles remain coupled to the melt in a closed-system degassing regime (Cassidy et al., 2018). When gas and melt are coupled with low melt volumes relative to the gas as expected for the picritic magmas, then extensive volatile-loss (i.e. $F_{Remaining} < 0.2$) would readily lead to wide ranges in $\delta^{34}S$ values of the residual melt measured in PGBs. This mechanism may be further facilitated by high surface-area/volume ratios of PGBs. Additionally, given that the volume of magma released during a single eruptive event was small (a few %) relative to the total source volume (Head and Wilson, 2017), it is further consistent that PGBs degassed with comparatively little isotopic effect on the residual magma chamber if it were to mix with other reservoirs.

It is also feasible that during exhumation of picritic magmas, bubble nucleation and subsequent volatile partitioning into the gas-phase was relatively more efficient compared to mare basalt melts. At shallow depths (~120 m), H_2 followed by H_2O and CO become volumetrically dominant in H-rich picritic melts (Newcombe et al., 2017; Sharp et al., 2013a). The presence of H_2-H_2O-CO-rich vapors in picritic magmas would result in an increasingly efficient volatile

346 partitioning into the gas-phase for Cl (Sigmarsson et al., 2020), and S as COS (Sato, 1976), and
347 H_2S (Rutherford et al., 2017). The efficient partitioning of S and Cl in the H-rich high gas-phase
348 volumes required to fragment the picritic magmas, alongside the high P/P_{Sat} values and associated
349 $\alpha'_{Kin(vapor\text{-}melt)}$ values >1 can readily explain the exceptionally low $\delta^{34}S$ values of PGBs.
350
351 ***Effusive: Mare Magmas.*** In comparison to PGBs, mare basalts show little variation in $\delta^{34}S$ values
352 which suggests that they did not undergo extensive S-loss, and/or that the integrated effective α'_{Kin}
353 values during degassing were close to 1 (i.e., minimal fractionation with $P/P_{sat} \sim 0.86$)(Fig. 9).
354 When the $\delta^{34}S$ values of PGBs are examined together with mare basalts in terms of S, F, and Cl
355 contents, the differing extents of degassing can be readily observed relative to the ranges measured
356 in melt inclusions (Fig. 10). Enigmatically, the mare basalts cooled much more slowly than the
357 quenched PGBs (1-20 ºC/h (Shearer et al., 1989) vs. 1-3 K/s (Saal et al., 2008; Zhang et al., 2019)).
358 The slow cooling rate of the mare basalts could feasibly result in further extents of degassing;
359 however, this idea is inconsistent with the limited ranges of Zn, S and Cl isotope compositions, as
360 well as comparably higher volatile contents (with exception to H) to volcanic glasses (Fig. 10).
361 Instead, the effusive eruption style which produced the mare basalts was seemingly
362 inefficient in the loss of volatile elements as mare magmas did not undergo the extensive low P
363 volatile separation within the volcanic conduit in the case for the picritic magmas. The thick mare
364 lava flows would form quench crusts serving to further limit volatile loss, such that there would
365 be minimal isotopic effects during degassing despite low pressure conditions on the lunar surface.
366 This idea is consistent with the fact that at low P/P_{Sat} values, even minimal extents of S-loss would
367 produce high $\delta^{34}S$ values which is not observed in the mare basalt data (Fig. 9). These observations
368 are also broadly consistent with bulk Cl and Zn isotope compositions which also exclude the

possibility of ideal vacuum degassing ($P/P_{Sat} \sim 0$) in bulk-rock mare basalts given the limited ranges in isotope values relative to the large kinetic isotope fractionation factors ($1000\ln\alpha_{Kinetic(gas-melt)}$ = -23 and -15‰ for HCl and Zn^o, respectively)(Gargano et al., 2020).

Despite the limited range of bulk-rock Zn, S and Cl isotope compositions relative to the large kinetic isotope fractionation factors, there is evidence for near-kinetic (vacuum or near-vacuum) degassing in late-forming and/or secondary phases contained in mare basalts. The $\delta^{37}Cl$ values of WSC in bulk-rock mare basalts are generally lighter than the corresponding SBC by 4.3 ‰ (Sharp et al., 2010; Gargano et al. 2020) which is explained by degassing and deposition of HCl or other Cl-bearing volatile phase into a near-vacuum, presumably along cracks in a mostly solidified basalt. The magnitude of this effect is even larger in the late-formed apatite grains where the degassing extent necessarily becomes very large to explain their high and wide-ranging $\delta^{37}Cl$ values (i.e., $F_{Remaining}$ approaches 0). For example, the $\delta^{37}Cl$ values of apatite in samples 15016 and 15556 (highly vesiculated low-Ti basalts) range from 6.5-19.1 and 28.9-36.4‰, respectively (Barnes et al., 2019; Faircloth et al., 2020). The $\delta^{34}S$ values of apatite are similarly wide-ranging in 15016 and 15556 from 14.6-29.5 and 2.7-10.6‰, respectively (Faircloth et al., 2020). These $\delta^{37}Cl$ and $\delta^{34}S$ values of apatite in 15016 and 15556 are in stark contrast to the bulk-rock $\delta^{37}Cl_{SBC}$ values of 2.14 and 10.57, and $\delta^{34}S$ values of 0.88 and 0.57‰, respectively. These discrepancies are best explained by kinetic isotope fractionation of S and Cl from the mare lavas under low P/P_{Sat} values along an open network of fractures in a nearly completely crystallized basalt. Similar ideas have been proposed in the formation of foam mounds in late-stage lava lakes where vesicles in the upper part of the mound ‘pop’ in vacuum (Wilson and Head, 2017a). Under these conditions and given the relatively small melt volumes retained in mesostasis regions where apatite crystallizes it

391 is feasible that the differences between the bulk-rock and apatite result from vacuum degassing of
392 apatite leading to their far higher and wide ranging $\delta^{34}S$ and $\delta^{37}Cl$ values.
393
394 **Implications:**
395 The long-standing difficulty in addressing the sources of volatile-element stable isotope
396 anomalies in lunar materials resulted from ambiguous relationships between isotopic compositions
397 and volatile contents (i.e. $\delta^{37}Cl$ and [Cl]). At present, however, a wealth of data has been generated
398 from numerous lithologies with different isotope systems, as well as target phases which further
399 elucidate this problem. While bulk-rock mare basalt measurements show limited variation in Zn,
400 S and Cl isotope compositions, *in situ* measurements of late-formed apatite show significantly
401 more variability (i.e., apatite, Figs. 1, 3). Additionally, a number of other lithologies such as Rusty
402 Rock (Day et al., 2019; Shearer et al., 2014), and lunar FANs (Gargano et al., 2020; Kato et al.,
403 2015) show significant variability and ranges of isotope values that are not seen in the bulk-rock
404 mare basalt suite.
405 These data suggest localized surface-related processes that produced anomalously low or
406 high isotope values for Zn, S, and Cl consistent with vacuum degassing. Bulk-rock low and high-
407 Ti mare basalts have elevated, yet restricted ranges of Zn, S, and Cl isotope compositions (relative
408 to the silicate Earth) that have been interpreted to reflect devolatilization during the Giant Impact
409 (Day et al., 2020; Gargano et al., 2020; Moynier et al., 2006; Paniello et al., 2012; Wing and
410 Farquhar, 2015). In contrast, the wide ranges in H, Cl, and S isotope compositions of lunar apatite
411 are interpreted to reflect isotope fractionation during magmatic degassing (Barnes et al., 2014;
412 Barnes et al., 2016; Boyce et al., 2015; Faircloth et al., 2020).

The similarity in bulk-rock $\delta^{66}Zn$, $\delta^{34}S$, and $\delta^{37}Cl$ values of low and high-Ti mare basalts, and generally high isotope values relative to Earth suggest that the Giant Impact and/or LMO degassing resulted in the heavy-isotope enrichment of Zn, S, and Cl in the mare source region. The restricted range of isotope values suggests that most mare basalts did not experience extensive post-eruptive volatile-loss, and/or that the integrated effective α'_{Kin} during degassing was ~ 1. While we cannot define the degree of isotope fractionation resulting solely from LMO degassing due to effective mantle mixing following mantle overturn, our data show that bulk-rock Zn, S, and Cl isotope compositions are identical between the low and high-Ti mare basalt suite such that no evidence exists to support this argument. Instead, the slightly elevated Zn, S and Cl isotope compositions of mare basalts suggest that the lunar mantle inherited a heavy-isotope enriched signature resulting from lunar formation (during the Giant Impact event) and remained largely unchanged throughout mare volcanism.

Conclusion:

In this work we show that the high Zn, S and Cl isotope values of the effusively erupted mare basalts are inherited from lunar formation and/or in addition to lunar magma ocean degassing. The bulk-rock Zn, S and Cl isotope compositions are not correlated, nor are they correlated with their respective volatile contents (i.e., $\delta^{37}Cl$ and [Cl]). This suggests that mare magmatism did not cause the heavy isotope enrichments relative to Earth. In contrast, the explosively erupted picritic glass beads exhibit a wide range of low $\delta^{34}S$ values inversely related to their S contents resulting from extensive degassing with high $P/P_{Sat} > 0.9$ and $\alpha'_{Kin} > 1$. The restricted range of $\delta^{34}S$ values of the mare basalts suggests that they were, in general, minimally degassed, and/or that their effective integrated isotope fractionation factor was near unity.

We are able to exclude the possibility of vacuum degassing affecting bulk-rock mare basalts given the limited range of Zn, S and Cl isotope values in lieu of the large kinetic isotope fractionation that would occur by this process. Mare lavas likely formed quench crusts and crystallized before significant volatile loss could occur in the bulk-rock under low P/P_{Sat} conditions on the lunar surface. In contrast, apatite in highly vesiculated basalts exhibit marked differences in $\delta^{34}S$ and $\delta^{37}Cl$ values when compared to the bulk-rock which suggests that apatite records extensive post-eruptive degassing under relatively lower P/P_{Sat} conditions. In total, these data provide further evidence for the idea that lunar volatile loss and volatile-element stable isotope fractionation largely occurred during lunar formation and that exceptionally high or low isotopic compositions likely resulted from localized phenomena influenced by reservoir effects.

Acknowledgements:

We thank NASA CAPTEM at NASA Johnson Space Center for the allocation of lunar samples measured in this work. This research was supported by a NASA Graduate Fellowship 17-AS&ASTAR17-0026 awarded to A.G. Funding for this work was also provided by the Science and Technology Facilities Council (STFC) to A.N.H. (STFC Planetary Origins and Developments: ST/M001318/1).

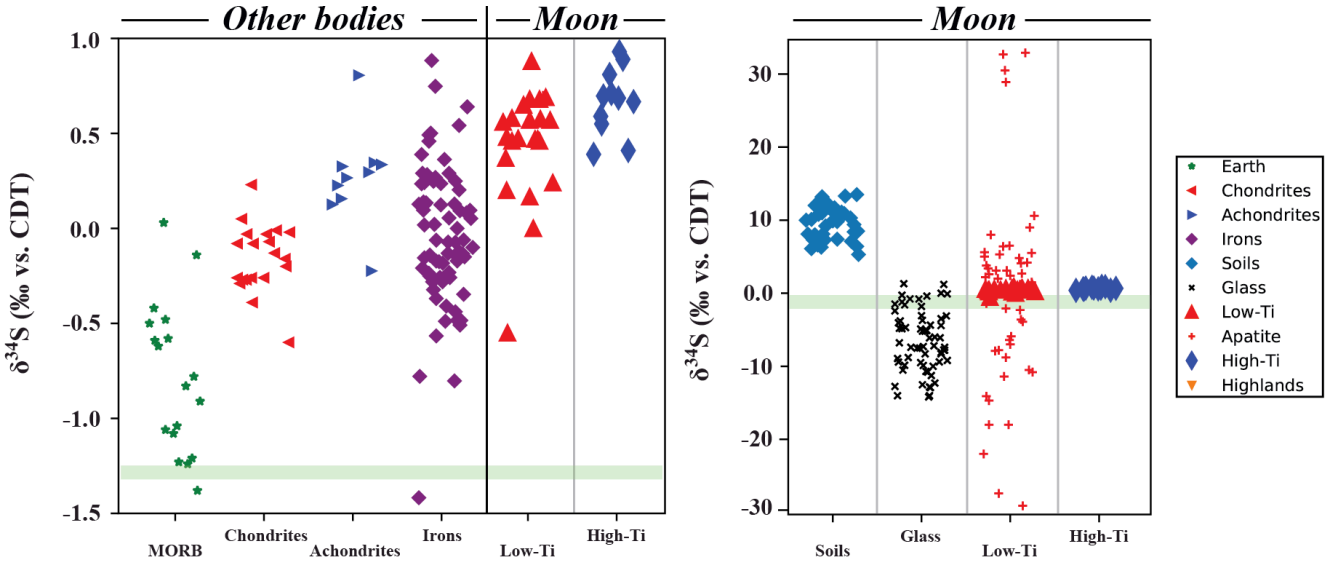

Figure 1: $\delta^{34}S$ (‰ vs. Canyon Diablo Troilite (CDT)) values of terrestrial and planetary materials. Data from (Antonelli et al., 2014; Faircloth et al., 2020; Gao and Thiemens, 1991; Gao and Thiemens, 1993a; Gao and Thiemens, 1993b; Labidi et al., 2013; Rees and Thode, 1974; Saal and Hauri, 2021; Wing and Farquhar, 2015; Wu et al., 2018). Green bar represents the estimated $\delta^{34}S$ value of the silicate Earth (Labidi et al., 2013).

459

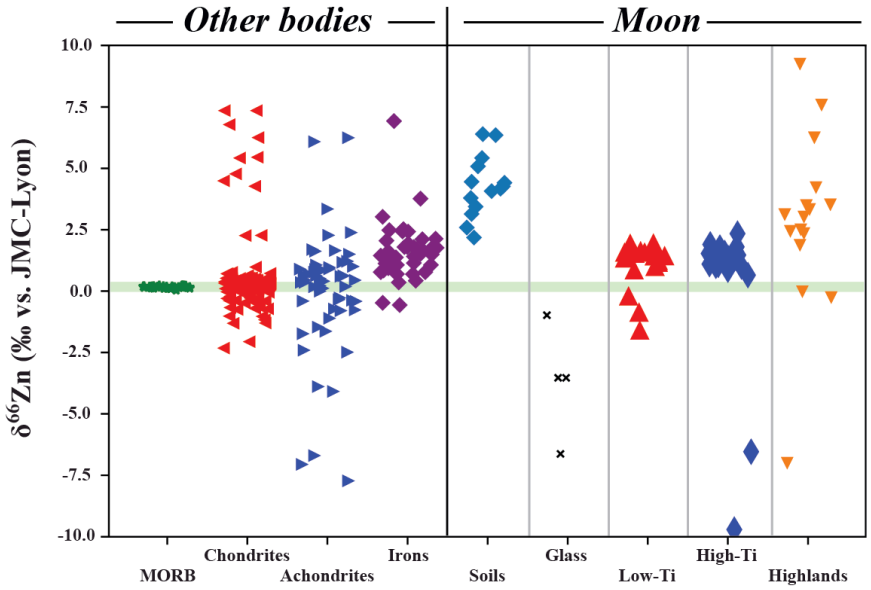

Figure 2: $\delta^{66}Zn$ (‰ vs. JMC-Lyon) values of terrestrial and planetary materials. Data from (Creech and Moynier, 2019; Day et al., 2020; Herzog et al., 2009; Moynier et al., 2006; Moynier et al., 2010; Moynier et al., 2007; Paniello et al., 2012; Sossi et al., 2018). Legend is same as Fig. 1. Green bar represents the estimated $\delta^{66}Zn$ value of the silicate Earth (Sossi et al., 2018).

460

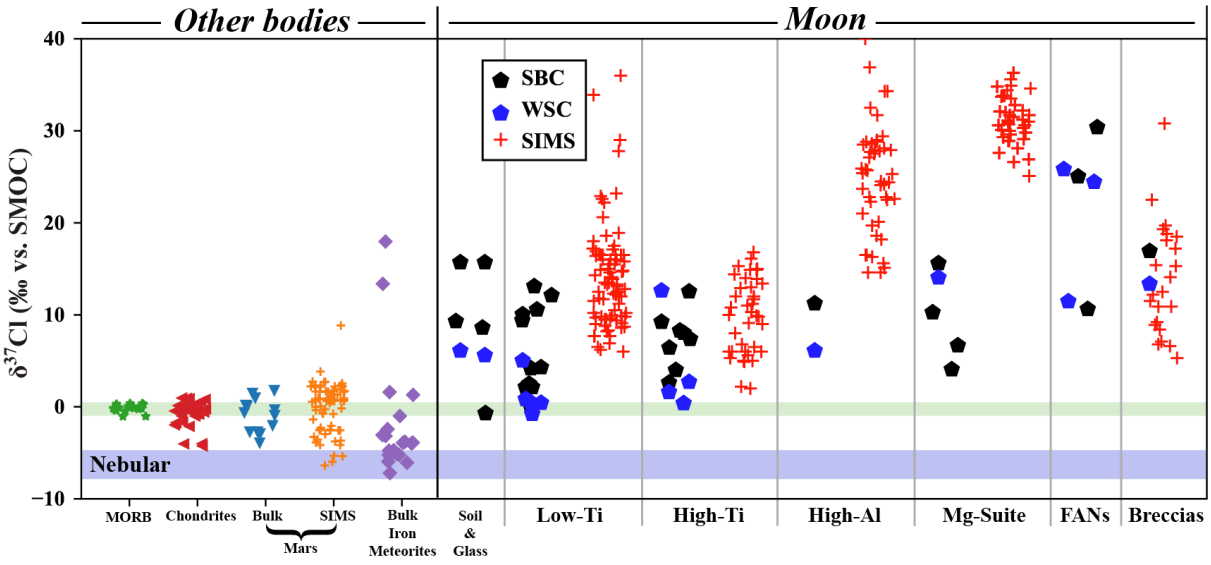

Figure 3: δ^{37}Cl (‰ vs. SMOC) of terrestrial and planetary materials. Figure adapted from Gargano et al., (2020). References can be found therein, in addition to Faircloth et al., (2020). Green bar represents the estimated δ^{37}Cl value of the silicate Earth (Sharp et al., 2013). Purple bar represents the estimated nebular value from Gargano & Sharp (2019) and Sharp et al., (2016).

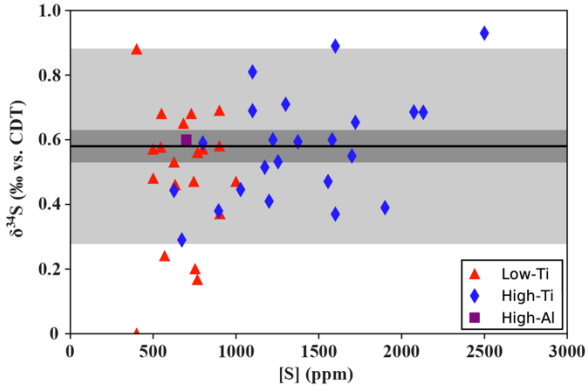

Figure 4: [S] (ppm) vs. δ^{34}S (‰ vs. CDT) of mare basalts. Light grey bar represents the 0.3‰ uncertainty in δ^{34}S values. Grey bar represents the 1 sigma standard deviation of the average δ^{34}S value of the mare basalt suite. Data sources: Rees & Thode (1972) and Wing & Farquhar (2015).

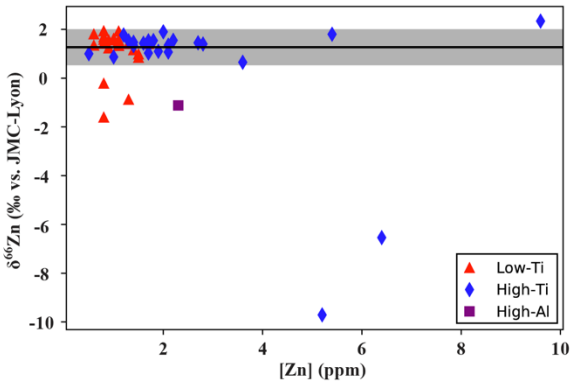

Figure 5: [Zn] (ppm) vs. δ^{66}Zn (‰ vs. JMC-Lyon) of mare basalts. Grey bar represents the 1 sigma standard deviation of the average δ^{66}Zn value of the mare basalt suite. Error is smaller than symbol size. Data sources: Day et al., (2020), Paniello et al., (2012) & Moynier et al., (2006).

461

462

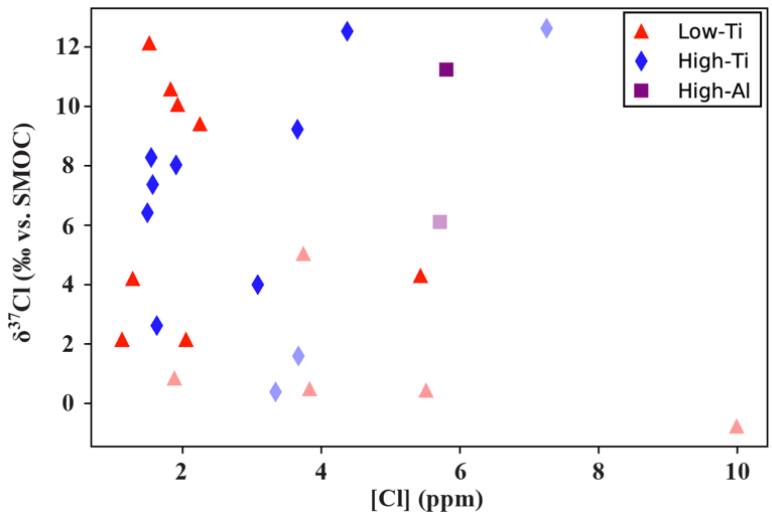

Figure 6: [Cl] (ppm) vs. δ^{37}Cl (‰ vs. SMOC) of mare basalts. SBC and WSC are plotted as solid and feint symbols respectively. Data from Gargano et al., (2020) and Sharp et al., (2010).

475

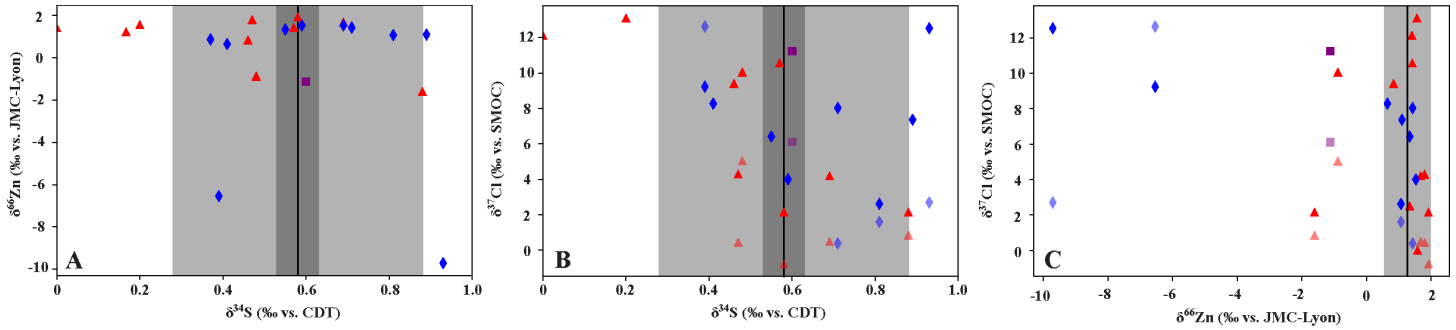

Figure 7: $\delta^{34}S$ vs. $\delta^{66}Zn$ (A), $\delta^{34}S$ vs. $\delta^{37}Cl$ (B), and $\delta^{66}Zn$ vs. $\delta^{37}Cl$ (C). Legend and faded and solid grey bars are the same as Figs. 4 & 5. Faded $\delta^{37}Cl$ symbols are $\delta^{37}Cl_{WSC}$.

476

477

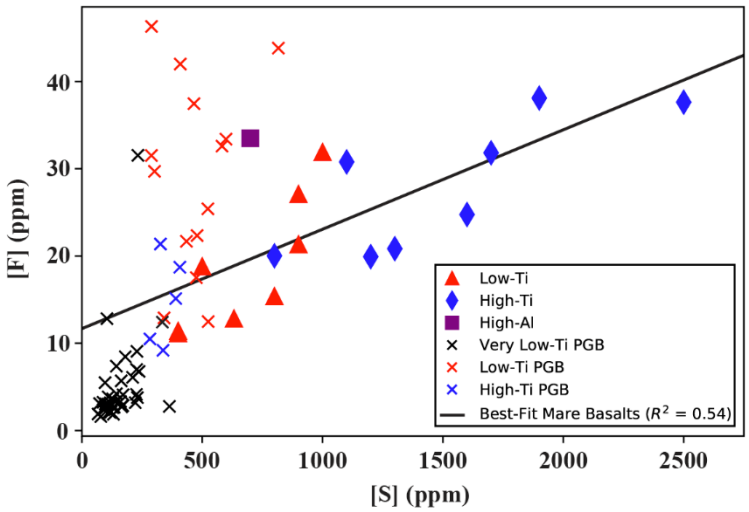

Figure 8: [S] (ppm) vs. [F] (ppm) of mare basalts and PGBs. Data from Gargano et al., (2020) and Saal & Hauri (2021).

478

479

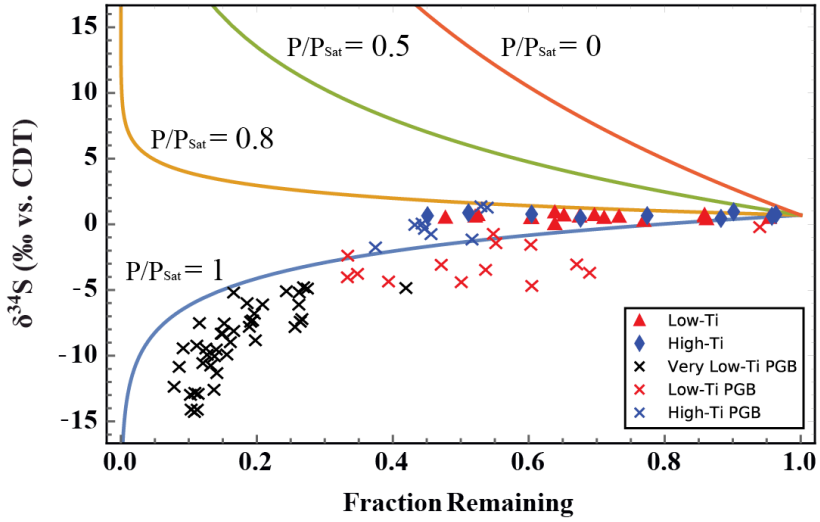

Figure 9: Rayleigh degassing regime of mare materials with initial $\delta^{34}S$ estimated at 0.7‰ with α'_{Kin} values from (Saal and Hauri, 2021; Wu et al., 2018). Fraction S remaining is calculated by estimates of initial S contents in source regions. Picritic glass beads are estimated relative to melt inclusions (74220 and 15016)(Chen et al., 2015; Ni et al., 2019). Mare basalts are relative to source region estimates (Bombardieri et al., 2005; Steenstra et al., 2018). A number of A15 basalts are excluded due to $F_{Remaining} > 1$ (15058, 15499, 15555, and 15556).

480

481

482

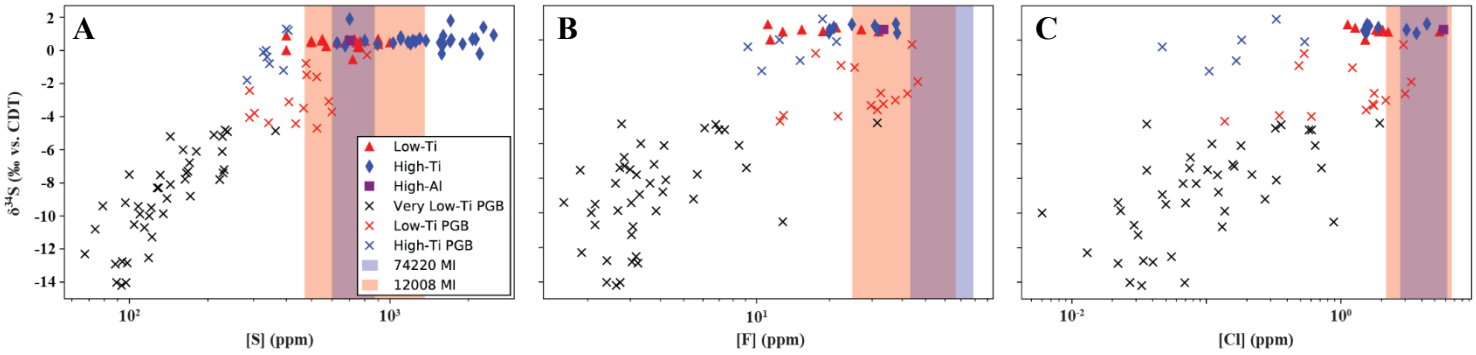

Figure 10: [S] (A), [F] (B), and $[Cl]_{SBC}$ (C)(ppm) vs $\delta^{34}S$ (‰ vs. CDT) of lunar mare basalts and PBGs. Vertical blue (74220) and red (12008) bars represent the ranges of S, F, and Cl contents in melt inclusions from Ni et al., (2019) and Chen et al., (2015).

483

484

485

486

487

488 **Data:**

489

Table 1: Zn and S contents and isotope compositions of mare basalts. Halogen contents and $\delta^{37}Cl$ values of this sample suite can be found in Gargano et al., (2020).

Sample	Lithology	[Zn] (ppm)	$\delta^{66}Zn$	2s	[S] (ppm)	$\delta^{34}S$	$\Delta^{33}S$	$\Delta^{36}S$
10017–405	High-Ti	6.7	-6.42	0.15	1900	0.39	-0.01	0.028
10017–400	High-Ti	5.5	-9.59	0.23	2500	0.93	0.013	-0.147
10020–255	High-Ti	1.3	1.55	0.06	1300	0.71	0.016	-0.119
10044–566	High-Ti	2.1	1.19	0.18	1100	0.81	-0.009	-0.191
12018–277	Low-Ti	1.5	-0.76	0.06	500	0.48	0.015	0.49
12054–13	Low-Ti	1.5	1.1	0.14				
12054–146	Low-Ti	0.8	1.92	0.13	900	0.58	0.005	-0.056
12054–150	Low-Ti	0.8	1.8	0.18	1000	0.47	0.001	-0.027
12063–343	Low-Ti	0.8	1.8	0.13	900	0.69	-0.009	0.076
14053–305	High-Al	1.6	-1	0.08	700	0.6	-0.01	-0.106
15016–240	Low-Ti	1	-1.49	0.12	400	0.88	-0.008	0.02
15535–165	Low-Ti	1	1.53	0.21	400	0	0.016	0.03
15556–258	Low-Ti	0.9	1.54	0.07	800	0.57	0.012	-0.017
70215–389	High-Ti	2.1	1.46	0.09	1700	0.55	0.007	0.26
70255–56	High-Ti	1.6	1.22	0.17	1600	0.89	-0.005	-0.086
71135–34	High-Ti	1.5	1.65	0.11	800	0.59	-0.011	-0.035
71546–22	High-Ti	1.8	1.54	0.27	1100	0.69	-0.008	-0.066
74275–355	High-Ti	1.2	1.64	0.17	1200	0.41	0.001	0.31
75035–249	High-Ti	1	0.87	0.75	1600	0.37	-0.006	0.23

490

491 **Supplemental Information:**

492 ***Notable Sample Description:***

493 10017**:** Sample 10017 is a fine-grained vesicular high-Ti-K mare basalt with high modal
494 mesostasis and vesicularity up to 20% (Beaty and Albee, 1978) and consisted of an exterior
495 (10017-405) and interior chip (10017-400). The interior of this sample was measured to have a
496 $\delta^{66}Zn$ value of -9.6‰ with 5.5 ppm Zn, with an exterior value of -6.42‰ and 6.7 ppm Zn. The
497 $\delta^{37}Cl_{SBC}$ of the interior and exterior was 9.23‰ and 12.53, respectively. Compared to other
498 samples, the WSC isotope composition of the interior is anomalously high at 12.63‰. The interior

of the sample contained 2500 ppm S with a $\delta^{34}S$ value of 0.93‰, with an exterior value of 0.39‰ and 1900 ppm S. The interior of this sample contains both lower Zn and Cl isotope values, yet higher S isotope values from the exterior. The abundances of S, Zn, and Cl are comparable in both the exterior and interior sections, and both are enriched in these elements relative to other high-Ti basalts. Lastly, we find it important to note that troilite within high-Ti-K basalts commonly occurs as spherules suggested to reflect sulfide immiscibility, and also occurs as globules within vesicles (Beaty and Albee, 1978).

15016 & 15556: Samples 15016 and 15556 are medium-grained olivine basalts with 1-5 mm vesicles which comprise up to 50% of the samples. The $\delta^{34}S$ values are comparable at 0.88 and 0.57‰, respectively with differing S contents of 400 and 800 ppm, respectively. In contrast, the $\delta^{66}Zn$ and $\delta^{37}Cl_{SBC}$ values are -1.49 and 1.54, and 2.14 and 10.6‰, respectively. The Cl_{SBC} and F contents of these samples are different at 1.12 and 1.83 ppm, and 11.1 and 15.4 ppm respectively. Goldberg et al. 1976 find F-rich coatings within the vesicles of these samples with 15016 containing 2x more F in the intervesicular region when compared to the vesicles, whereas 15556 is measured to contain similar F contents in both regions.

Samples:

In this work we chose to analyze 19 mare basalts with sample aliquots designated from partnering chips for Cl, Zn and S isotope compositions. Our chosen samples encompass the low-Ti, and high-Ti mare basalt sub-groupings (Neal and Taylor, 1992). We also measured the interiors and exteriors of some notable samples such as 10017 and 12054 to address sample heterogeneity and surface-relate isotopic anomalies. Two Apollo 15 basalts 15016 and 15556 were also measured due to high vesicularity.

Methods:

Chlorine:

Samples for Cl isotope measurements were performed as follows following the method of Sharp et al. (2010): Samples were crushed and leached with deionized water to obtain water-soluble chloride (WSC). Residual leachates were then rinsed again to remove any residual water-soluble chloride fraction, then dried and loaded into quartz tubes. Structurally-bound chloride was then extracted via pyrohydrolysis where the powdered sample was melted in a stream of water vapor, passed through a condensing column and finally collected in the condensed water. The WSC and SBC fractions were processed in the same manner for isotope measurements: Solutions are reacted with 5 mL 50% HNO_3 for 24 hours to degas sulfur, followed by the addition of 1 mL 0.4M $AgNO_3$ to precipitate AgCl overnight. AgCl is then filtered and loaded into 6mm diameter pyrex tubes. The tubes are evaculated and 10 μL CH_3I is added prior to flame-sealing. Sealed tubes are then reacted at 80°C for 48 hours to produce CH_3Cl as an analyte. Chlorine isotopes were measured on a Delta^{PLUS}XL in continuous flow mode at the University of New Mexico. Sample reproducibility has been shown to be ±0.25‰. The isotopic composition of Cl is reported relative to Standard Mean Ocean Chloride (SMOC)

$$\delta^{37}Cl(‰) = \left(\frac{\frac{^{37}Cl}{^{35}Cl}_{Sample}}{\frac{^{37}Cl}{^{35}Cl}_{SMOC}} - 1 \right) * 1000$$

Zinc:

Zn isotope measurements were performed at the University of Oxford by S. Hopkins and A. Halliday. Samples were transferred to metal-free centrifuge tubes and cleaned with DI water for 2 hours. Samples were then dried and powdered in an agate mortar. Powder aliquots were then measured to obtain approximately 0.25 ug Zn (around 20-140 mg of sample). Hotplate dissolution

544 was then performed using HF-HNO_3 and HCl over multiple days. Sample dissolution was
545 complete when no undissolved components remained. Small aliquots of each sample dissolution
546 was then weighed and mixed with a ^{64}Zn-^{67}Zn double spike (5.10025 ppm, (Arnold et al., 2010))
547 and equilibrated over 48 hours at 60°C. Solutions were then passed through an anion-exchange
548 column before analysis by MC-ICPMS to determine the Zn concentrations. These concentrations
549 were then used to calculate the appropriate mass ratios of spike/sample solution. Appropriated
550 spiked samples were then passed through the anion-exchange column twice to purify Zn from
551 interfering elements. Zn isotope compositions were then measured using a *Nu instruments* Plasma
552 HR mass spectrometer. Masses 62, 64, 66, 67, 67.5, and 68 were measured simultaneously. Masses
553 62 and 67.5 were used for $^{64}Ni^{+}$ and Ba^{2+} corrections. Exterior sample washes typically had
554 negligible Zn contents (<0.2 ng). USGS reference materials BCR2, BHVO2, and BIR1a were
555 prepared in the same manner as the lunar samples. The isotopic composition of Zn is reported
556 relative to JMC-Lyon

557 $$\delta^{66}Zn(‰) = \left(\frac{\frac{^{66}Zn}{^{64}Zn}_{Sample}}{\frac{^{66}Zn}{^{64}Zn}_{JMC-Lyon}} - 1 \right) * 1000$$

558 ***Sulfur:***

559 Sulfur isotopes were measured at the University of Maryland by J. Dottin and J. Farquhar. Samples
560 were firstly coarsely crushed in a steel mortar and pestle and subsequently powdered in an agate
561 mortar using <5mL ethanol to reduce dust loss. Ethanol-powder slurry was then quantitatively
562 transferred to reactions vessels. Flasks were filled with 20mL 5M HCl and 20mL of Cr(II) Chloride
563 solution and heated to sub boiling temperatures with a continuous flow of N_2 (Canfield et al.,
564 1986). The reaction proceeds for ~3 hours as the release of H_2S that is first carried through a water
565 trap to capture acid vapors and second through an $AgNO_3$ trap where S is precipitated as Ag_2S.

Precipitated Ag_2S was then centrifuged and transferred to 1.5ml Eppendorf tubes and rinsed 6 times with Milli-Q.

After rinsing, samples were dried for ~ 2 hours at 70 degrees C and weighed for extraction yields to estimate S concentrations. The Ag_2S was then transferred into clean aluminum foil, loaded into Ni reaction vessels and reacted with approximately 10x stoichiometric excess of F_2 at 250°C overnight yielding SF_6 as an analyte. Analyte gas was separated from non-condensable gases by liquid-N_2 traps. HF was then separated from SF_6 by an ethanol-liquid N_2 trap. SF_6 was then purified by passing through a 12.5 A Hasep Q gas chromatography column. Purified SF6 was lastly analyzed in dual inlet mode on a MAT 253 mass spectrometer. The isotopic composition of sulfur is normalized using the same method as Antonelli et al. (2014) and Dottin et al. (2018) where samples are first normalized to bracketed analyses of IAEA-S1 from each analytical session and subsequently normalized to the value IAEA-S1 relative to Canyon Diablo Troilite (CDT) reported in Antonelli et al. (2014) which places IAEA-S1 at $\delta^{33}S = -0.091$, $\delta^{34}S = -0.401$, $\delta^{36}S = -1.558$, $\Delta^{33}S = 0.116$, $\Delta^{36}S = -0.796$ (Dottin et al. 2020).

$$\delta^{34}S(‰) = \left(\frac{\frac{^{34}S}{^{32}S}_{Sample}}{\frac{^{34}S}{^{32}S}_{CDT}} - 1 \right) * 1000$$

References:

Antonelli, M.A. et al., 2014. Early inner solar system origin for anomalous sulfur isotopes in differentiated protoplanets. Proceedings of the National Academy of Sciences, 111(50): 17749-17754.

Arnold, T. et al., 2010. Measurement of zinc stable isotope ratios in biogeochemical matrices by double-spike MC-ICPMS and determination of the isotope ratio pool available for plants from soil. Analytical and bioanalytical chemistry, 398(7-8): 3115-3125.

Bali, E., Hartley, M., Halldórsson, S., Gudfinnsson, G., Jakobsson, S., 2018. Melt inclusion constraints on volatile systematics and degassing history of the 2014–2015 Holuhraun eruption, Iceland. Contributions to Mineralogy and Petrology, 173(2): 1-21.

Barnes, J.J., Franchi, I.A., McCubbin, F.M., Anand, M., 2019. Multiple reservoirs of volatiles in the Moon revealed by the isotopic composition of chlorine in lunar basalts. Geochimica et Cosmochimica Acta, 266: 144-162.

Barnes, J.J. et al., 2014. The origin of water in the primitive Moon as revealed by the lunar highlands samples. Earth and Planetary Science Letters, 390: 244-252.
Barnes, J.J. et al., 2016. Early degassing of lunar urKREEP by crust-breaching impact(s). Earth and Planetary Science Letters, 447: 84-94.
Beaty, D., Albee, A., 1978. Comparative petrology and possible genetic relations among the Apollo 11 basalts, Lunar and Planetary Science Conference Proceedings, pp. 359-463.
Bombardieri, D.J., Norman, M.D., Kamenetsky, V.S., Danyushevsky, L.V., 2005. Major element and primary sulfur concentrations in Apollo 12 mare basalts: The view from melt inclusions. Meteoritics & Planetary Science, 40(5): 679-693.
Boyce, J. et al., 2018. Chlorine isotopes in the low-Ti basalts, and the early loss of volatiles from the Earth-Moon system. Earth and Planetary Science Letters, 500: 205-214.
Boyce, J.W. et al., 2015. The chlorine isotope fingerprint of the lunar magma ocean. Science Advances, 1: 8 pp.
Brett, R. et al., 1971. Apollo 12 igneous rocks 12004, 12008, 12009, and 12022: A mineralogical and petrological study, Lunar and Planetary Science Conference Proceedings, pp. 301.
Canfield, D.E., Raiswell, R., Westrich, J.T., Reaves, C.M., Berner, R.A., 1986. The use of chromium reduction in the analysis of reduced inorganic sulfur in sediments and shales. Chemical geology, 54(1-2): 149-155.
Canup, R.M., Visscher, C., Salmon, J., Fegley Jr, B., 2015. Lunar volatile depletion due to incomplete accretion within an impact-generated disk. Nature Geosci, 8(12): 918-921.
Cassidy, M., Manga, M., Cashman, K., Bachmann, O., 2018. Controls on explosive-effusive volcanic eruption styles. Nature communications, 9(1): 1-16.
Charnoz, S. et al., 2021. Tidal pull of the Earth strips the proto-Moon of its volatiles. Icarus, 364: 114451.
Chen, H., Savage, P.S., Teng, F.-Z., Helz, R.T., Moynier, F., 2013. Zinc isotope fractionation during magmatic differentiation and the isotopic composition of the bulk Earth. Earth and Planetary Science Letters, 369: 34-42.
Chen, Y. et al., 2015. Water, fluorine, and sulfur concentrations in the lunar mantle. Earth and Planetary Science Letters, 427: 37-46.
Creech, J., Moynier, F., 2019. Tin and zinc stable isotope characterisation of chondrites and implications for early Solar System evolution. Chemical Geology, 511: 81-90.
Davis, F.A., Humayun, M., Hirschmann, M.M., Cooper, R.S., 2013. Experimentally determined mineral/melt partitioning of first-row transition elements (FRTE) during partial melting of peridotite at 3 GPa. Geochimica et Cosmochimica Acta, 104: 232-260.
Day, J.M., Moynier, F., Shearer, C.K., 2017. Late-stage magmatic outgassing from a volatile-depleted Moon. Proceedings of the National Academy of Sciences, 114(36): 9547-9551.
Day, J.M., Sossi, P.A., Shearer, C.K., Moynier, F., 2019. Volatile distributions in and on the Moon revealed by Cu and Fe isotopes in the 'Rusty Rock'66095. Geochimica et Cosmochimica Acta, 266: 131-143.
Day, J.M., van Kooten, E.M., Hofmann, B.A., Moynier, F., 2020. Mare basalt meteorites, magnesian-suite rocks and KREEP reveal loss of zinc during and after lunar formation. Earth and Planetary Science Letters, 531: 115998.
de Moor, J.M. et al., 2013. Sulfur degassing at Erta Ale (Ethiopia) and Masaya (Nicaragua) volcanoes: Implications for degassing processes and oxygen fugacities of basaltic systems. Geochemistry, Geophysics, Geosystems, 14(10): 4076-4108.
Ding, S., Hough, T., Dasgupta, R., 2018. New high pressure experiments on sulfide saturation of high-FeO∗ basalts with variable TiO2 contents–Implications for the sulfur inventory of the lunar interior. Geochimica et Cosmochimica Acta, 222: 319-339.
Dottin III, J.W., Farquhar, J., Labidi, J., 2018. Multiple sulfur isotopic composition of main group pallasites support genetic links to IIIAB iron meteorites. Geochimica et Cosmochimica Acta, 224: 276-281.
Elkins-Tanton, L.T., Burgess, S., Yin, Q.-Z., 2011. The lunar magma ocean: Reconciling the solidification process with lunar petrology and geochronology. Earth and Planetary Science Letters, 304(3–4): 326-336.
Faircloth, S., Anand, M., Franchi, I., Zhao, X., Russell, S., 2020. Multiple sulfur isotopic reservoirs in the Moon and implications for the evolution of planetary interiors.
Gao, X., Thiemens, M.H., 1991. Systematic study of sulfur isotopic composition in iron meteorites and the occurrence of excess 33S and 36S. Geochimica et Cosmochimica Acta, 55(9): 2671-2679.
Gao, X., Thiemens, M.H., 1993a. Isotopic composition and concentration of sulfur in carbonaceous chondrites. Geochimica et Cosmochimica Acta, 57(13): 3159-3169.
Gao, X., Thiemens, M.H., 1993b. Variations of the isotopic composition of sulfur in enstatite and ordinary chondrites. Geochimica et Cosmochimica Acta, 57(13): 3171-3176.

650 Gargano, A., Sharp, Z., 2019. The chlorine isotope composition of iron meteorites: Evidence for the Cl isotope
651 composition of the solar nebula and implications for extensive devolatilization during planet formation.
652 Meteoritics & Planetary Science, 54(7): 1619-1631.
653 Gargano, A. et al., 2020. The Cl isotope composition and halogen contents of Apollo-return samples. Proceedings of
654 the National Academy of Sciences, 117(38): 23418-23425.
655 Gauthier, P.J., Sigmarsson, O., Gouhier, M., Haddadi, B., Moune, S., 2016. Elevated gas flux and trace metal
656 degassing from the 2014–2015 fissure eruption at the Bárðarbunga volcanic system, Iceland. Journal of
657 Geophysical Research: Solid Earth, 121(3): 1610-1630.
658 Green, D., Ringwood, A., Hibberson, W., Ware, N., 1975. Experimental petrology of Apollo 17 mare basalts, Lunar
659 and Planetary Science Conference Proceedings, pp. 871-893.
660 Hauri, E.H., Saal, A.E., Rutherford, M.J., Van Orman, J.A., 2015. Water in the Moon's interior: Truth and
661 consequences. Earth and Planetary Science Letters, 409: 252-264.
662 Hauri, E.H., Weinreich, T., Saal, A.E., Rutherford, M.C., Van Orman, J.A., 2011. High pre-eruptive water contents
663 preserved in lunar melt inclusions. Science, 333(6039): 213-215.
664 Head, J.W., Wilson, L., 2017. Generation, ascent and eruption of magma on the Moon: New insights into source
665 depths, magma supply, intrusions and effusive/explosive eruptions (Part 2: Predicted emplacement processes
666 and observations). Icarus, 283: 176-223.
667 Herzog, G., Moynier, F., Albarède, F., Berezhnoy, A., 2009. Isotopic and elemental abundances of copper and zinc in
668 lunar samples, Zagami, Pele's hairs, and a terrestrial basalt. Geochimica et Cosmochimica Acta, 73(19):
669 5884-5904.
670 Hess, P.C., Parmentier, E., 1995. A model for the thermal and chemical evolution of the Moon's interior: Implications
671 for the onset of mare volcanism. Earth and Planetary Science Letters, 134(3-4): 501-514.
672 Hiesinger, H., Head, J., Wolf, U., Jaumann, R., Neukum, G., 2011. Ages and stratigraphy of lunar mare basalts: A
673 synthesis. Recent advances and current research issues in lunar stratigraphy, 477: 1-51.
674 Kato, C., Moynier, F., Valdes, M.C., Dhaliwal, J.K., Day, J.M., 2015. Extensive volatile loss during formation and
675 differentiation of the Moon. Nature communications, 6: 7617.
676 Kesson, S., 1975. Mare basalt petrogenesis, Origins of Mare Basalts and their Implications for Lunar Evolution, pp.
677 81.
678 Labidi, J., Cartigny, P., 2016. Negligible sulfur isotope fractionation during partial melting: Evidence from Garrett
679 transform fault basalts, implications for the late-veneer and the hadean matte. Earth and Planetary Science
680 Letters, 451: 196-207.
681 Labidi, J., Cartigny, P., Moreira, M., 2013. Non-chondritic sulphur isotope composition of the terrestrial mantle.
682 Nature, 501(7466): 208-211.
683 Labidi, J., Farquhar, J., Alexander, C.O.D., Eldridge, D., Oduro, H., 2017. Mass independent sulfur isotope signatures
684 in CMs: Implications for sulfur chemistry in the early solar system. Geochimica et Cosmochimica Acta, 196:
685 326-350.
686 Lock, S.J., Bermingham, K.R., Parai, R., Boyet, M., 2020. Geochemical constraints on the origin of the Moon and
687 preservation of ancient terrestrial heterogeneities. Space Science Reviews, 216(6): 1-46.
688 Lock, S.J. et al., 2018. The origin of the Moon within a terrestrial synestia. Journal of Geophysical Research: Planets,
689 123(4): 910-951.
690 Longhi, J., 1992. Experimental petrology and petrogenesis of mare volcanics. Geochimica et Cosmochimica Acta,
691 56(6): 2235-2251.
692 Longhi, J., Walker, D., Hays, J.F., 1972. Petrography and crystallization history of basalts 14310 and 14072, Lunar
693 and Planetary Science Conference Proceedings, pp. 131.
694 Ma, C., Liu, Y., 2019. Discovery of a zinc-rich mineral on the surface of lunar orange pyroclastic beads. American
695 Mineralogist: Journal of Earth and Planetary Materials, 104(3): 447-452.
696 Marini, L., Moretti, R., Accornero, M., 2011. Sulfur isotopes in magmatic-hydrothermal systems, melts, and magmas.
697 Reviews in Mineralogy and Geochemistry, 73(1): 423-492.
698 McCubbin, F.M., Barnes, J.J., 2020. The chlorine-isotopic composition of lunar KREEP from magnesian-suite
699 troctolite 76535. American Mineralogist: Journal of Earth and Planetary Materials, 105(8): 1270-1274.
700 Moynier, F., Albarède, F., Herzog, G., 2006. Isotopic composition of zinc, copper, and iron in lunar samples.
701 Geochimica et Cosmochimica Acta, 70(24): 6103-6117.
702 Moynier, F. et al., 2010. Volatilization induced by impacts recorded in Zn isotope composition of ureilites. Chemical
703 Geology, 276(3-4): 374-379.

704 Moynier, F., Blichert-Toft, J., Telouk, P., Luck, J.-M., Albarède, F., 2007. Comparative stable isotope geochemistry
705 of Ni, Cu, Zn, and Fe in chondrites and iron meteorites. Geochimica et Cosmochimica Acta, 71(17): 4365-
706 4379.
707 Neal, C.R., Taylor, L.A., 1992. Petrogenesis of mare basalts: A record of lunar volcanism. Geochimica et
708 Cosmochimica Acta, 56(6): 2177-2211.
709 Newcombe, M. et al., 2019. Effects of pH2O, pH2 and fO2 on the diffusion of H-bearing species in lunar basaltic
710 liquid and an iron-free basaltic analog at 1 atm. Geochimica et Cosmochimica Acta, 259: 316-343.
711 Newcombe, M. et al., 2017. Solubility of water in lunar basalt at low pH2O. Geochimica et Cosmochimica Acta, 200:
712 330-352.
713 Ni, P., Zhang, Y., Chen, S., Gagnon, J., 2019. A melt inclusion study on volatile abundances in the lunar mantle.
714 Geochimica et Cosmochimica Acta, 249: 17-41.
715 Nie, N.X., Dauphas, N., 2019. Vapor drainage in the protolunar disk as the cause for the depletion in volatile elements
716 of the Moon. The Astrophysical Journal Letters, 884(2): L48.
717 Paniello, R.C., Day, J.M., Moynier, F., 2012. Zinc isotopic evidence for the origin of the Moon. Nature, 490(7420):
718 376.
719 Potts, N.J., Bromiley, G.D., Brooker, R.A., 2021. An experimental investigation of F, Cl and H2O mineral-melt
720 partitioning in a reduced, model lunar system. Geochimica et Cosmochimica Acta, 294: 232-254.
721 Rai, V.K., Jackson, T.L., Thiemens, M.H., 2005. Photochemical mass-independent sulfur isotopes in achondritic
722 meteorites. Science, 309(5737): 1062-1065.
723 Rees, C., Thode, H., 1974. Sulfur concentrations and isotope ratios in Apollo 16 and 17 samples, Lunar and Planetary
724 Science Conference Proceedings, pp. 1963-1973.
725 Renggli, C., King, P., Henley, R., Norman, M., 2017. Volcanic gas composition, metal dispersion and deposition
726 during explosive volcanic eruptions on the Moon. Geochimica et Cosmochimica Acta, 206: 296-311.
727 Renggli, C.J., Klemme, S., 2021. Experimental investigation of Apollo 16 “Rusty Rock” alteration by a lunar
728 fumarolic gas. Journal of Geophysical Research: Planets, 126(2): e2020JE006609.
729 Richet, P., Bottinga, Y., Javoy, M., 1977. A review of hydrogen, carbon, nitrogen, oxygen, sulphur, and chlorine stable
730 isotope fractionation among gaseous molecules. Annual Review of Earth and Planetary Science, 5: 65-110.
731 Rutherford, M.J., Head, J.W., Saal, A.E., Hauri, E., Wilson, L., 2017. Model for the origin, ascent, and eruption of
732 lunar picritic magmas. American Mineralogist, 102(10): 2045-2053.
733 Saal, A.E., Hauri, E.H., 2021. Large sulfur isotope fractionation in lunar volcanic glasses reveals the magmatic
734 differentiation and degassing of the Moon. Science Advances, 7(9): eabe4641.
735 Saal, A.E. et al., 2008. Volatile content of lunar volcanic glasses and the presence of water in the Moon’s interior.
736 Nature, 454(7201): 192-195.
737 Sato, M., 1976. Oxygen fugacity and other thermochemical parameters of Apollo 17 high-Ti basalts and their
738 implications on the reduction mechanism, Lunar and planetary science conference proceedings, pp. 1323-
739 1344.
740 Schauble, E.A., Rossman, G.R., Taylor, H.P., 2003. Theoretical estimates of equilibrium chlorine-isotope
741 fractionations. Geochimica et Cosmochimica Acta, 67: 3267-3281.
742 Sharp, Z.D., McCubbin, M., Shearer, C.K., 2013a. A hydrogen-based oxidation mechanism relevant to planetary
743 formation. Earth and Planetary Science Letters, 380: 88-97.
744 Sharp, Z.D. et al., 2013b. The chlorine isotope composition of chondrites and Earth. Geochimica et Cosmochimica
745 Acta, 107: 189-204.
746 Sharp, Z.D., Shearer, C.K., McKeegan, K.D., Barnes, J.D., Wang, Y.Q., 2010. The Chlorine Isotope Composition of
747 the Moon and implications for an anhydrous mantle. Science, 329: 1050-1053.
748 Shearer, C., Papike, J., 1993. Basaltic magmatism on the Moon: A perspective from volcanic picritic glass beads.
749 Geochimica et Cosmochimica Acta, 57(19): 4785-4812.
750 Shearer, C., Papike, J., Simon, S., Shimizu, N., 1989. An ion microprobe study of the intra-crystalline behavior of
751 REE and selected trace elements in pyroxene from mare basalts with different cooling and crystallization
752 histories. Geochimica et Cosmochimica Acta, 53(5): 1041-1054.
753 Shearer, C. et al., 2014. Chlorine distribution and its isotopic composition in “rusty rock” 66095. Implications for
754 volatile element enrichments of “rusty rock” and lunar soils, origin of “rusty” alteration, and volatile element
755 behavior on the Moon. Geochimica et Cosmochimica Acta, 139: 411-433.
756 Shearer, C.K. et al., 2006. Thermal and Magmatic Evolution of the Moon. Reviews in Mineralogy and Geochemistry,
757 60: 365-518.
758 Sigmarsson, O., Moune, S., Gauthier, P.-J., 2020. Fractional degassing of S, Cl and F from basalt magma in the
759 Bárðarbunga rift zone, Iceland. Bulletin of Volcanology, 82(7): 1-8.

760 Snyder, G., Borg, L., Nyquist, L., Taylor, L., 2000. Chronology and isotopic constraints on lunar evolution. Origin of
761 the Earth and Moon: 361-395.
762 Snyder, G.A., Taylor, L.A., Neal, C.R., 1992. A chemical model for generating the sources of mare basalts: Combined
763 equilibrium and fractional crystallization of the lunar magmasphere. Geochimica et Cosmochimica Acta,
764 56(10): 3809-3823.
765 Sossi, P.A., Nebel, O., O'Neill, H.S.C., Moynier, F., 2018. Zinc isotope composition of the Earth and its behaviour
766 during planetary accretion. Chemical Geology, 477: 73-84.
767 Steenstra, E. et al., 2018. Evidence for a sulfur-undersaturated lunar interior from the solubility of sulfur in lunar melts
768 and sulfide-silicate partitioning of siderophile elements. Geochimica et Cosmochimica Acta, 231: 130-156.
769 Tang, H., Young, E., 2020. Evaporation from the Lunar Magma Ocean Was Not the Mechanism for Fractionation of
770 the Moon's Moderately Volatile Elements. The Planetary Science Journal, 1(2): 49.
771 van Kan Parker, M., Mason, P.R., Van Westrenen, W., 2011. Trace element partitioning between ilmenite, armalcolite
772 and anhydrous silicate melt: Implications for the formation of lunar high-Ti mare basalts. Geochimica et
773 Cosmochimica Acta, 75(15): 4179-4193.
774 van Kooten, E.M., Moynier, F., Day, J.M., 2020. Evidence for transient atmospheres during eruptive outgassing on
775 the Moon. The Planetary Science Journal, 1(3): 67.
776 Walker, D., Kirkpatrick, R., Longhi, J., Hays, J., 1976. Crystallization history of lunar picritic basalt sample 12002:
777 Phase-equilibria and cooling-rate studies. Geological Society of America Bulletin, 87(5): 646-656.
778 Walker, D., Longhi, J., Hays, J.F., 1972. Experimental petrology and origin of Fra Mauro rocks and soil, Lunar and
779 Planetary Science Conference Proceedings, pp. 797.
780 Wang, Z.-Z. et al., 2017. Zinc isotope fractionation during mantle melting and constraints on the Zn isotope
781 composition of Earth's upper mantle. Geochimica et Cosmochimica Acta, 198: 151-167.
782 Webster, J., Kinzler, R., Mathez, E., 1999. Chloride and water solubility in basalt and andesite melts and implications
783 for magmatic degassing. Geochimica et Cosmochimica Acta, 63(5): 729-738.
784 Wieczorek, M.A. et al., 2013. The crust of the Moon as seen by GRAIL. Science, 339(6120): 671-675.
785 Wilson, L., Head, J., 2018. Controls on lunar basaltic volcanic eruption structure and morphology: Gas release patterns
786 in sequential eruption phases. Geophysical Research Letters, 45(12): 5852-5859.
787 Wilson, L., Head, J.W., 2017a. Eruption of magmatic foams on the Moon: Formation in the waning stages of dike
788 emplacement events as an explanation of "irregular mare patches". Journal of Volcanology and Geothermal
789 Research, 335: 113-127.
790 Wilson, L., Head, J.W., 2017b. Generation, ascent and eruption of magma on the Moon: New insights into source
791 depths, magma supply, intrusions and effusive/explosive eruptions (Part 1: Theory). Icarus, 283: 146-175.
792 Wing, B.A., Farquhar, J., 2015. Sulfur isotope homogeneity of lunar mare basalts. Geochimica et Cosmochimica Acta,
793 170: 266-280.
794 Wu, N., Farquhar, J., Dottin III, J.W., Magalhães, N., 2018. Sulfur isotope signatures of eucrites and diogenites.
795 Geochimica et Cosmochimica Acta, 233: 1-13.
796 Zhang, L. et al., 2019. Reassessment of pre-eruptive water content of lunar volcanic glass based on new data of water
797 diffusivity. Earth and Planetary Science Letters, 522: 40-47.
798 Zolotov, M.Y., Matsui, T., 2002. Chemical models for volcanic gases on Venus, Lunar and Planetary Science
799 Conference, pp. 1433.
800